ARTICLE OPEN

Check for updates

Biodegradable elastomeric circuit boards from citric acid-based polyesters

Brendan L. Turner[1], Jack Twiddy[1], Michael D. Wilkins[2], Srivatsan Ramesh[3], Katie M. Kilgour[3], Eleo Domingos[1], Olivia Nasrallah[1], Stefano Menegatti[3,4]✉ and Michael A. Daniele[1,2]✉

Recyclable and biodegradable microelectronics, i.e., "green" electronics, are emerging as a viable solution to the global challenge of electronic waste. Specifically, flexible circuit boards represent a prime target for materials development and increasing the utility of green electronics in biomedical applications. Circuit board substrates and packaging are good dielectrics, mechanically and thermally robust, and are compatible with microfabrication processes. Poly(octamethylene maleate (anhydride) citrate) (POMaC) – a citric acid-based elastomer with tunable degradation and mechanical properties – presents a promising alternative for circuit board substrates and packaging. Here, we report the characterization of Elastomeric Circuit Boards (ECBs). Synthesis and processing conditions were optimized to achieve desired degradation and mechanical properties for production of stretchable circuits. ECB traces were characterized and exhibited sheet resistance of 0.599 Ω cm^{-2}, crosstalk distance of <0.6 mm, and exhibited stable 0% strain resistances after 1000 strain cycles to 20%. Fabrication of single layer and encapsulated ECBs was demonstrated.

npj Flexible Electronics (2023)7:25 ; https://doi.org/10.1038/s41528-023-00258-z

INTRODUCTION

Electronic waste (e-waste) represents a significant environmental challenge with about 40 million metric tons generated per year and projections estimate increases in the future[1]. Aside from environmental concerns about dangerous heavy metals, e-waste also contributes to losses of precious metals, of which there is a finite supply. Passive components and circuit boards are the largest category of e-waste, representing about 16.8 million tons of total e-waste in 2021[2]. The importance of developing sustainable and degradable materials cannot be understated, in regards to realizing a sustainable electronics ecosystem. Alternative to the traditional "long-lasting" electronics paradigm, transient or biodegradable electronics are being developed to reduce e-waste[3] and for biologically and environmentally interfacing applications[4–6]. Popular material components for biodegradable electronics include paper-based electronics[7,8], biocompatible metals[9,10], natural and synthetic polymers[11,12] and thin-film inorganics[13,14]. These materials can degrade in a controlled manner in the presence of a specific trigger condition[15] including biomolecules, moisture, temperature changes, light, or mechanical force. The ideal biodegradable electronic device has a programmable lifespan, degrades fully into non-toxic components, and still provides rigorous electronic functionality.

The next generation of electronic devices will by characterized by the synthesis of biodegradable and biomimetic approaches for material and electronics development. Electronic materials that incorporate both stretchable and degradable characteristics[16–21] provide traditional electronic functions while offering new functionalities including ability to survive mechanical deformations, conform to curvilinear surfaces, and match the stiffness of various biological tissues[22]. This presents innovative opportunities for the design of mechanically robust, transient systems with expanded applications in healthcare[23–25], energy harvesting[26], soft robotics[27–29], and consumer electronics[30,31].

Synthetic, biodegradable elastomers are an attractive candidate material for these applications. Many strategies have been used to confer elastic properties into non-stretchable conducting materials employing structures using out-of-plane[32] or in-plane[33] geometries. However, almost all these approaches rely on an elastomeric substrate to absorb or dissipate the mechanical strain[34–37]. Additionally, approaches to create elastic conductors[38], semi-conductors[39], and dielectrics[15] have used composite techniques combining electronically active materials like silver nanoparticles with elastomers[40]. Furthermore, elastomers have a long history of applications in tissue engineering due to wide-ranging tensile moduli to match target tissues, and ensured biocompatibility and biodegradability[41]. These synergistic properties position elastomers at the forefront of materials development for the next generation of stretchable and biodegradable electronics.

Many stretchable electronic technologies composed of non-degradable elastomers have been presented in literature, including thermoplastic polyurethanes used as substrate and composite material[42,43], polyurethane sponges[44], conductive, elastomeric spandex fibers[45], and poly(dimethylsiloxane) (PDMS). PDMS in particular has been used extensively as substrate and conductive elastic composite material for stretchable electronics applications including stretchable electrodes[46], supercapacitors[47], sweat sensors[48], and epicardial cardiac stimulation patches[49]. These example materials and devices highlight some of the potential applications for elastic devices. Stretchable PDMS electrodes have shown promising properties with limited fatigue at up to 100% strain and strain cycle resistance after 10,000 cycles[50]. Despite these impressive examples, a suitable elastic alternative to non-degradable and bioinert PDMS is required to achieve the next generation of devices.

[1]Joint Department of Biomedical Engineering, North Carolina State University and University of North Carolina, Chapel Hill, 911 Oval Dr., Raleigh, NC 27695, USA. [2]Department of Electrical & Computer Engineering, North Carolina State University, 890 Oval Dr., Raleigh, NC 27695, USA. [3]Department of Chemical and Biomolecular Engineering, North Carolina State University, 911 Partners Way, Raleigh, NC 27695, USA. [4]Biomanufacturing Training and Education Center (BTEC), North Carolina State University, 850 Oval Dr, Raleigh, NC 27606, USA. ✉email: smenega@ncsu.edu; mdaniel6@ncsu.edu

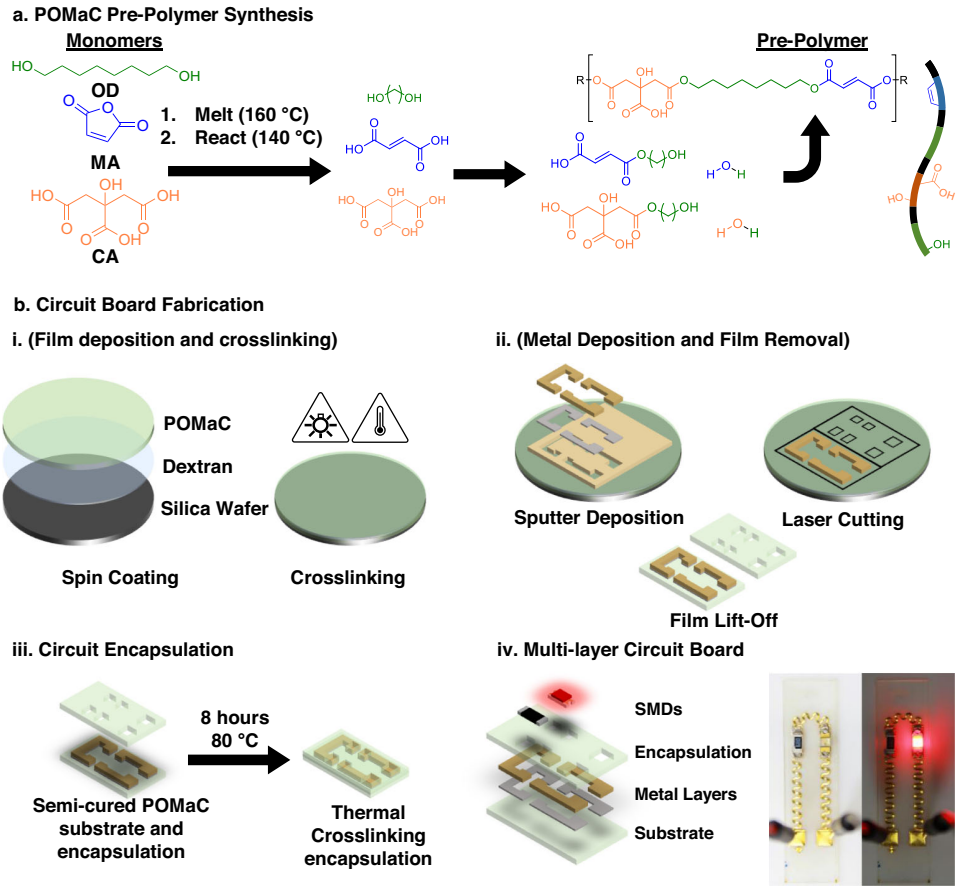

Fig. 1 Overview. a POMaC pre-polymer is synthesized in a polycondensation reaction from 1,8-octanediol (OD), maleic anhydride (MA), and citric acid (CA). **b** Elastomeric Circuit Board fabrication. i. Thin films of POMaC are prepared by spin coating and then crosslinked. ii. Next, physical vapor deposition of conductive traces through a shadow mask is used to pattern circuits before films are laser cut and removed from the substrate. iii. POMaC circuit boards are then encapsulated by thermally crosslinking a POMaC top layer to the metallized bottom layer. iv. Surface-mount devices are attached by soldering to openings in the encapsulation layer.

One such set of elastomers are the citric acid derivatives[41,51–53] that were first presented as elastic tissue scaffolds for soft tissue engineering. The original formulation was composed of citric acid and a diol that could be degraded by hydrolysis at varying rates depending on post-processing[54]. Since their initial presentation, citric acid elastomers have been complexed with a variety of monomers that partially replaced citric acid or the diol including sebacic acid[55], 1,4-cyclohexanedimethanol[56], and others[57–59] to target different physiochemical properties and bioactivity. These elastomers have been used as biocompatible interfaces for polytetrafluorethylene vascular grafts[60], as components in electrospun composites to increase elasticity[61], as scaffolds for retinal tissue engineering[62] and for other applications in soft tissue and bone engineering.

Poly(octamethylene maleate (anhydride) citrate) (POMaC) is a citric acid-based elastomer that provides tunable mechanical properties, biocompatibility, biodegradation[63], demonstrated strain cycle resistance[64,65], and potential for robust performance under mechanical deformation and adhesion to curvilinear surfaces[66,67]. POMaC is produced by polycondensation reaction of non-toxic and inexpensive monomers: 1,8-octane diol, maleic anhydride, and citric acid[63] (Fig. 1a). The produced pre-polymer can then by crosslinked using photo and/or thermal crosslinking through the unsaturated hydrocarbons in the backbone or the pendant carboxylic acid and hydroxyl groups (Fig. 1a), respectively, to fine tune mechanical and degradation properties. These same functional groups offer potential for chemical modification of the polymer before or after crosslinking. The polymer undergoes degradation via surface erosion in physiological conditions that breaks ester bonds between monomers and results in a linear loss of mechanical properties during degradation[65,68]. The material was initially developed for tissue engineering applications and has been demonstrated as cell scaffolding material[63] and as an injectable tissue scaffold[69]. POMaC has also shown potential for development of structures via injection molding[70] and microfabrication strategies[71,72] to enhance cell culture outcomes. The elastomer has also been used in microphysiological systems to model cardiac fibrosis[73] and screen cardiac drugs[74]. The elasticity, hydrophobicity, and available pendant groups in POMaC have been utilized, in conjunction with additives to enhance photocrosslinking, for the development of tough underwater adhesives for biomedical applications[66]. POMaC has also been developed for use in implantable sensors as outer packaging and strain resistance components for an implantable strain and pressure sensor[64,65]. The soft and elastic properties of POMaC were also leveraged in an arterial pulse sensor where POMaC was used as the arterial interfacing material to prevent tissue irritation and allow artery expansion[67].

Boutry et al. have shown examples of biodegradable devices employing POMaC as a packaging material in two devices, including an arterial pulse sensor[67] and a strain and pressure sensor[47]. In these works, POMaC was adopted owing to its biocompatibility, biodegradability, and mechanical properties that promote favorable interactions with soft tissues. However, in both devices the conductive material was adhered to other substrates: the arterial pulse sensor used PLLA as substrate for magnesium

structures, a microstructured PGS as a dielectric for pulse detection, and PHB/PHV as a bottom layer; likewise, the strain and pressure sensors operate with similar design principles, only using POMaC as the top and bottom packaging layers. In spite of the promising nature of POMaC, this material has thus far been used only as encapsulation/packaging and for tissue culture. In this work we seek to expand its functionality by presenting its application as a biodegradable elastomeric circuit board substrate. Thus, unlike prior literature where POMaC merely serves as a component of a larger device, this study presents a fabrication method, material and electrical characterizations, and functional examples of this polymer as a substrate material for elastomeric circuit boards. Although previous work has incorporated POMaC as an active biomaterial component, no previous work has investigated the potential of POMaC for electronic substrates. In this work, POMaC is demonstrated and characterized for use as an Elastomeric Circuit Board (ECB) substrate, and corresponding microfabrication methods are developed (Fig. 1b). Three POMaC pre-polymers from different monomer feed ratios were synthesized and characterized for monomer content based on feed ratio and reaction times. The pre-polymers are thermally stable under 200 °C and peak degradation occurs at 400 °C. Based on the increased branching and the potential for post-functionalization POMaC-6 (3:2:5 MA:CA:OD) was further characterized to determine its material properties. Additionally, the degradation and mechanical properties were characterized with respect to crosslinking conditions. POMaC 6 films had tensile moduli ranging from 0.4–2.3 MPa and elongation at break ranging from 20–56%. Due to the low tensile modulus and high elongation at break, thermally crosslinked POMaC-6 was used to fabricate circuit boards and then characterized for electrical properties. The sheet resistance and crosstalk losses of conductive traces on POMaC-6 substrates were 0.599 Ω cm^{-2} and −25 dBs, respectively. Trace impedance was monitored across a frequency sweep from 1 Hz to 5 MHz and showed expected behavior with constant phase and magnitude until 100 kHz where a slight increase in impedance was exhibited. Encapsulated metal traces on POMaC-6 substrates were characterized over 1000 cycles of 0–20% strain with peak $R/R_0 \sim 87$. Lastly, biomedical applications for POMaC-based ECBs were demonstrated. The potential for chemical functionalization was demonstrated by patterning films with fluorescent molecules and encapsulated circuits were demonstrated operating under strain and in simulated physiological conditions.

RESULTS & DISCUSSION

Pre-polymer synthesis & characterization

Three monomer feed ratios were used, POMaC-4 (P4), POMaC-6 (P6), and POMaC-8 (P8), for the synthesis of the POMaC pre-polymer variants (ca. Table 1). Each pre-polymer was prepared by a melt polycondensation reaction with the corresponding ratio of monomers, purified by precipitation from dioxane into water, frozen, and lyophilized. The molar ratio of monomers for each pre-polymer was determined using ^{1}H-NMR (d6-DMSO-400 MHz) (Fig. 2a): δ = 6.0–7.0 (m, 2H), 3.97–4.08 (m, 1H), 3.57 (s, 8H), 3.37 (t, 2H), 2.6–3.0 (m, 4H), 2.5 (m, 6H), 1.58 (s, 4H), 1.27–1.4 (group, 8H). The peaks (f) between 6–7 ppm were attributed to the –C<u>H</u>=C<u>H</u>– from maleic anhydride. The peaks (a) between 2.6–3.0 ppm were attributed to the –C<u>H</u>$_2$– from the citric acid. The peaks (c) at 1.58 ppm were attributed to the –C<u>H</u>$_2$–C<u>H</u>$_2$–OH from 1,8-octane diol. Using these characteristic monomer peaks, the pre-molar ratio of monomers was characterized as a function of reaction time (Fig. 2b) by calculation of the ratio of normalized signal areas of characteristic proton peaks for each monomer (e.g., for maleic anhydride (a/4)/(a/4 + f/2 + c/4)) with final monomer molar ratios reported in Table 1. For all reaction times evaluated, 1,8-octane diol is under-represented in the as-synthesized pre-polymer. After 5 h, both citric acid and maleic anhydride incorporation approach their feed ratio value in the as-synthesized pre-polymer. For all further experiments, a reaction time of 5 h was used for pre-polymer synthesis.

Table 1. Feed ratios for POMaC pre-polymers and the NMR calculated molar ratio for each pre-polymer.

Pre-polymer	Feed			Observed		
	MA	CA	OD	MA	CA	OD
POMaC-4	2	3	5	2.01	3.20	4.79
POMaC-6	3	2	5	3.12	2.26	4.61
POMaC-8	4	1	5	4.28	1.17	4.54

MA maleic anhydride, *CA* citric acid, *OD* 1,8-octanediol.

Each pre-polymer was also characterized using thermogravimetric analysis (TGA) to assess molecular weight distribution and thermal degradation behavior of the pre-polymers (*cf*. Fig. 2c). A volatile mass loss (~10%) was observed below 200 °C for each pre-polymer, which was attributed to dioxane and water remaining from the purification process. Around 200 °C, there is additional mass loss up to ~8% in P4, 14% in P6, and 20% in P8, which is inversely correlated to citric acid content in the monomer feed ratio. Increased citric acid content in the monomer feed ratio increases pre-polymer chain branching[75]. Accordingly, the mass loss at 200 °C is attributed to thermal degradation of lesser branched, lower molecular weight pre-polymer chains. This is further corroborated by the derivative TGA curve (DTG), as a low-temperature shoulder is observed across the bulk degradation region (265–475 °C). The shoulder occurs at higher temperatures with increasing citric acid in the monomer feed ratio. Peak thermal degradation is exhibited at 400 °C for all feed ratios. No thermal degradation of the polymer is expected below 200 °C, and POMaC films exhibited no weight loss under 200 °C with a more singular degradation profile at ~300 °C. (Supplementary Fig. 1), as compared to the pre-polymer.

POMaC film fabrication and characterization

Use of POMaC for tissue engineering typically involves highly porous networks with increased maleic anhydride content (1 CA: 4 MA: 5 OD) to enable fast photocrosslinking[72]. While porous and photocrosslinked films can enable increased efficiency of cell, protein, and drug loading, photocrosslinked POMaC films result in sticky surfaces not amenable to microfabrication methods[65]. Accordingly, the P6 pre-polymer (3CA :2 MA:5 OD) was selected for further development of elastomeric circuit boards. The P6 pre-polymer offers increased capacity for thermal crosslinking by ester bond formation, while providing supplemental unsaturated hydrocarbons for photocrosslinking and functionalization.

Film fabrication. POMaC provides for two crosslinking modes, whereby both photocrosslinking by backbone carbon-carbon double bonds and thermal crosslinking by ester-bond formation between pendant carboxylic acid and hydroxyl groups can be used to tune material properties. P6 pre-polymer was prepared with 5% w/w photoinitiator (Irgacure 2959). P6 films were deposited by spin coating (Fig. 1b i), crosslinked by a combination of photocrosslinking and thermal crosslinking (Fig. 1b i), laser cut to appropriate dimensions, and removed by water submersion (Fig. 1b ii). Appropriate spin coating conditions are necessary to achieve a uniform film. In this work, film thickness was not controllable by simple variation of spin coating parameters, so a spreading agent (e.g., dioxane) would be necessary to control film thickness. After spin coating, photocrosslinking was performed by exposure to UV light ($\lambda_{peak} = 365$ nm) for a dose of 0, 3, or

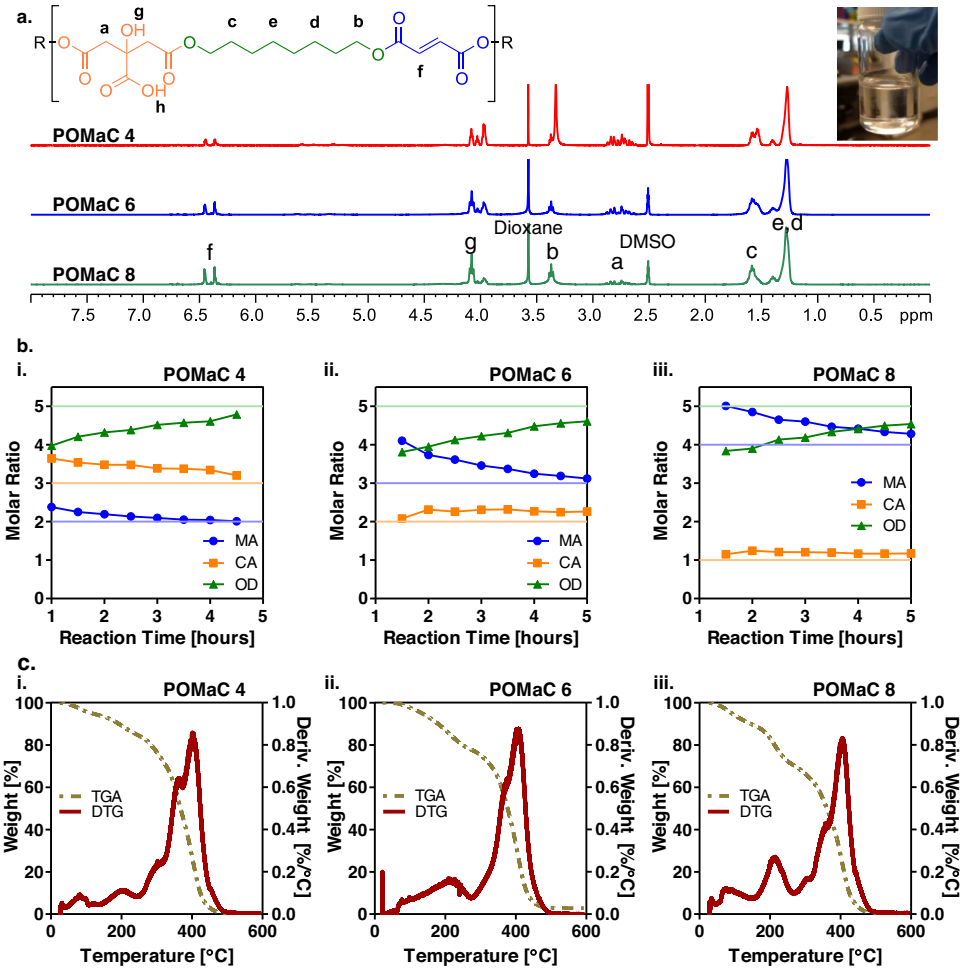

Fig. 2 POMAC pre-polymer characterization. a ^{1}HNMR spectra for POMaC pre-polymer variants P4, P6, and P8 (top to bottom) with annotated peaks corresponding to protons in the labeled structure of a typical POMaC chain. **b** Plots of substituent monomer molar ratios for POMaC pre-polymer variants P4 (i), P6 (ii), and P8 (iii) (left to right) at various times during the pre-polymer synthesis. **c** TGA (left axis) and derivative plots (right axis) showing thermal degradation properties of POMaC pre-polymer variants P4 (i), P6 (ii), and P8 (iii).

Table 2. Crosslinking conditions and physical properties for POMaC films.

UV (J·cm^{-2})	80 °C (h)	Sol (%)	Swell (%) (DMSO)	E (MPa)	σ (MPa)	Elongation (%)
6	24	32.8 ± 1.24	404 ± 44.3	0.860 ± 0.027	0.170 ± 0.016	22.7 ± 2.21
6	36	–	–	1.26 ± 0.059	0.251 ± 0.013	23.3 ± 2.01
6	48	–	–	2.30 ± 0.059	0.412 ± 0.015	20.4 ± 2.47
3	36	28.6 ± 1.15	313 ± 28.7	0.539 ± 0.056	0.177 ± 0.014	44.4 ± 4.32
3	48	–	–	1.18 ± 0.027	0.355 ± 0.044	38.0 ± 5.52
0	48	26.4 ± 1.11	366 ± 29.3	0.395 ± 0.026	0.164 ± 0.015	56.6 ± 4.23

Numbers are reported as mean ± standard error.
UV ultraviolet dosage, *sol* solution, *DMSO* dimethyl sulfoxide, *E* tensile modulus, *σ* tensile strength.

6 J·cm^{-2}. After photocrosslinking, P6 films were subsequently baked at 80 °C for 24, 36, or 48 h. To differentiate between crosslinking conditions, variants are named UV dose – hours crosslinked. For instance, a P6 film exposed to 3 J·cm^{-2} and baked for 48 h is referred to as P6 3–48. Film forming conditions are summarized in Table 2. For a UV dosage of 6 J·cm^{-2} each baking condition resulted in removable films. For a UV dosage of 3 J·cm^{-2}, thermal crosslinking for 24 h did not produce removable films. For films produced without photocrosslinking, neither 24 nor 36 h of thermal crosslinking resulted in free-standing films.

Swelling and degradation characterization. The solution percent (sol %) of crosslinked films was found to range between 26–33% (Table 2) with increasing sol % as ester crosslinking was reduced. Crosslinking conditions had no statistically significant effects on sol %. To determine relative swelling behavior as a function of crosslinking conditions, swelling was performed in DMSO at room temperature where swelling of crosslinked films ranged from 313 to 404% (Table 2). Crosslinking conditions had no significant effect on swelling in DMSO. The mass swelling behavior of P6 0–48 films were examined by a kinetic swelling study (Fig. 3a ii): *(i)* in DI water

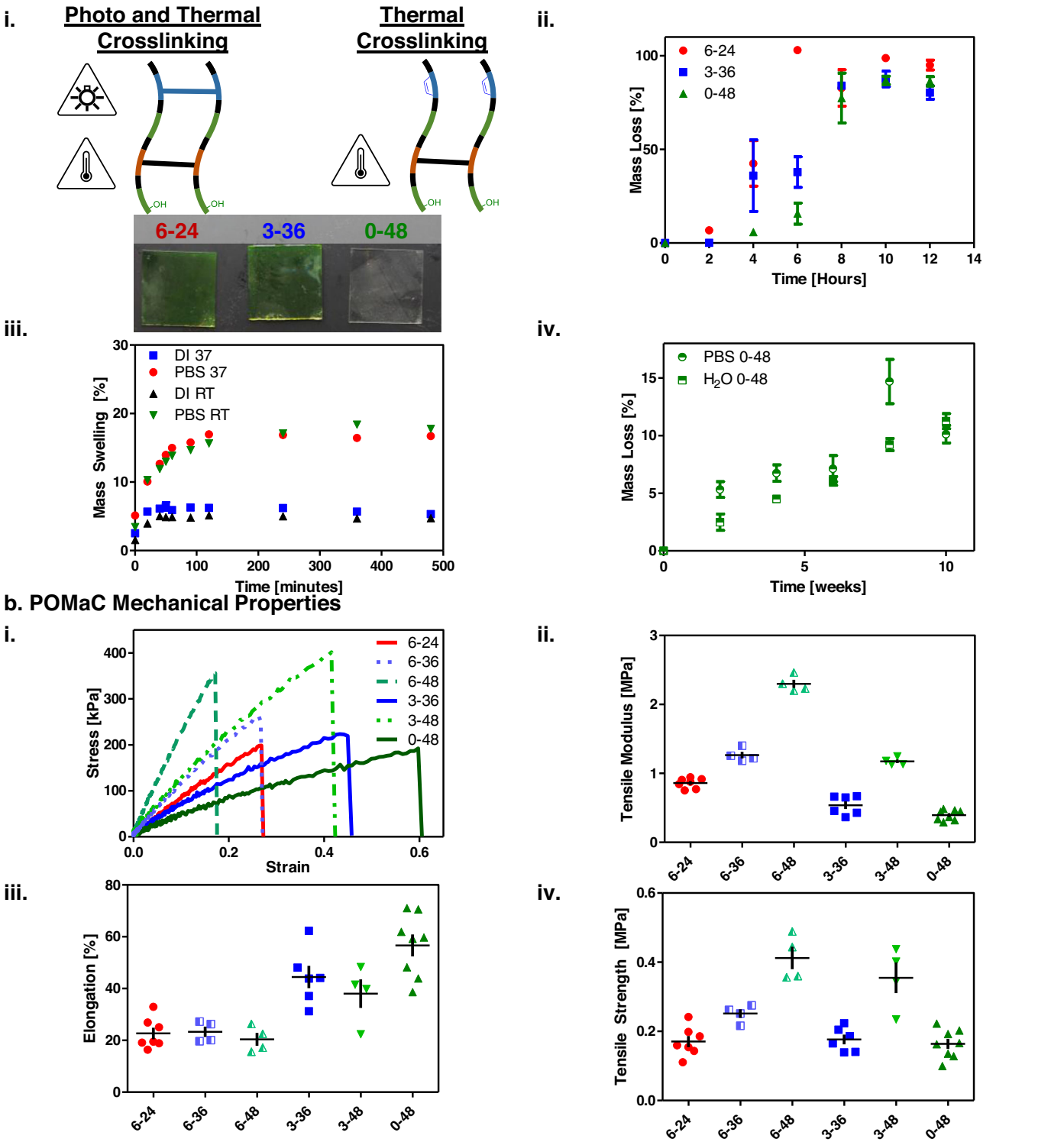

Fig. 3 Material characterization of POMaC 6 films. a Degradation and swelling properties. i. The pre-polymer can be crosslinked using either photo or thermal crosslinking into films that have different appearances and physical properties. ii. 0.05 M NaOH accelerated degradation curves for three POMaC crosslinking conditions. iii. Kinetic swelling behavior of POMaC 0–48 in DI water and PBS at 37 °C and 25 °C. iv. Long-term degradation of POMaC 0–48 films in PBS and DI water. **b** Mechanical properties. i. Representative stress-strain curves for crosslinked POMaC films. ii. Tensile modulus of crosslinked POMaC films. iii. Elongation percentage of crosslinked POMaC films. iv. Tensile strength of crosslinked POMaC films. Error bars depict standard error of the mean.

at room temperature, a swelling equilibrium of ~4% was reached after 40 min of immersion; *(ii)* in DI water at 37 °C, a swelling equilibrium of ~5% was reached after 20 min of immersion. No change in diameter was observed after 24 h of immersion in DI water (Supplementary Fig. 7); *(iii)* in PBS at room temperature, a swelling equilibrium of ~17% was reached after 240 min of immersion (*note:* a diameter change of ~0.8 mm was observed after 24 h, as shown in Supplementary Fig. 5); finally, *(iv)* in PBS at 37 °C, swelling equilibrium of ~17% was reached after 120 min of immersion. From a fabrication standpoint, the limited swelling observed in DI water seems to permit long-term soaks for lift-off procedures, whereas PBS swelling may be a concern in applications that require processing steps in ionic solutions.

The degradation properties of substrates are important for the development of recyclable or transient electronics. Ideal materials should have tunable degradation rates for different applications, allowing for a range of device lifespans without compromising functionality[76]. For example, a single-use biosensor should degrade rapidly after sensing has concluded, while a surgical implant to monitor wound healing should last until the end of the healing process[53]. To characterize degradation rates for different crosslinking conditions, an accelerated degradation was performed in 0.05 M sodium hydroxide (NaOH) at room temperature. The POMaC polymer is crosslinked mostly by ester bonds and NaOH has been used previously to examine hydrolytic degradation rates in accelerated conditions[77–79]. Of the three conditions evaluated, 0–48 films had the greatest resistance to hydrolytic degradation, which can be observed by the lower degradation rate shown by the 0–48 films (green triangles) compared to the other crosslinking conditions (Fig. 3a ii). Additionally, a long-term degradation study was performed using P6 0–48 films in DI water and PBS over 10 weeks at 37 °C (Fig. 3a iii-iv). Swelling in both systems was also monitored and a markedly slower swelling rate was observed in DI water compared to PBS (Fig. 3a iii). In PBS, the films swelled to 40% after 4 weeks and swelling rates leveled off at 60% after 8 weeks. In DI water, the films swelled less rapidly, reaching about 20% swelling at 10 weeks. The mass loss observed was linear by Runs test and showed mass loss rate of ~0.02% and ~1.7% per week in DI water and PBS, respectively (Fig. 3b iv).

Mechanical characterization. Stretchable electronics enable a wider range of applications for bio-interfaced devices. For instance, conformal stretchable materials offer the possibility of more comfortable and functional wearables placed in contact with human skin[80] or as implantable devices[81]. Conformal contact increases the reliability of sensor measurements and soft materials cause less overall tissue irritation[82]. Ideal circuit boards for stretchable electronics should have tunable tensile modulus and stretchability as requirements will vary between applications. Here, the mechanical properties of P6 films were examined as a function of crosslinking conditions and results summarized in Table 2.

P6 films exhibited a wide spectrum of mechanical properties with tensile moduli ranging from 0.4–2.3 MPa, elongation at break ranging from 20–56%, and tensile strength ranging from 0.17–0.41 MPa. A variety of stress-strain curves were observed for POMaC films processed under different crosslinking conditions (Fig. 3b i). The tensile modulus (Fig. 3b ii) showed the greatest response to changing crosslinking conditions, showing statistically significant increases with increased photocrosslinking duration and with increased thermal crosslinking duration. Elongation percent (Fig. 3b iii) did not significantly change with thermal crosslinking but showed significant decreases with increased photocrosslinking. Tensile strength (Fig. 3b iv) showed significant increases with increasing thermal and photocrosslinking.

Holding constant the degree of photocrosslinking and increasing thermal crosslinking (e.g., comparing films that received 6 J·cm^{-2}) resulted in statistically significant increases in tensile modulus and strength, while elongation percentage remained stable. Holding constant the degree of thermal crosslinking while increasing photocrosslinking (comparing films baked for 48 and 36 h) resulted in statistically significant increases in tensile modulus and strength and decreases in elongation percentage. As expected, combinations of crosslinking conditions can also achieve similar desired outcomes, e.g. 3–36 and 0–48 conditions exhibit statistically equivalent mechanical properties.

POMaC-ECB characterization

Printed circuit boards (PCBs) are an essential component of complex, multi-component devices, allowing a variety of electronic components to be electrically interconnected in a way that minimizes total device volume. Many research groups have developed flexible PCBs for applications in wearable devices[83–86]. However, the same groups note that incorporation of elastic properties are necessary for truly bio-inspired systems that can match the local stiffness and stretchability of biological tissues. For example, skin is not only flexible, but can withstand large strains with elastic recovery[80,87]. Accordingly, we fabricated and characterized POMaC-based elastomeric circuit boards (ECBs) for their fundamental electrical properties, i.e., sheet resistance, electrical impedance at various frequencies, potential crosstalk distance limitations, as well as performance under repeated tensile strain.

For all fabricated elastomeric circuit boards, 0–48 crosslinked films were utilized owing to their low tensile modulus (0.395 MPa) and high elongation percent at break (56%) compared to the other crosslinking conditions characterized. Briefly, circuit boards were fabricated by sputter deposition of a titanium (Ti) or chromium (Cr) adhesion layer and a gold (Au) conductive layer through a shadow mask onto crosslinked POMaC films (Fig. 1d ii). Following metal deposition, the films were laser cut and detached from the substrate by dissolving the underlying water-soluble sacrificial layer. (Fig. 1d ii). The DC resistance of circuit traces fabricated using these methods was observed to be unchanged after film lift-off. For encapsulated circuit boards, the films were thermally crosslinked for 40 h before deposition. After deposition, the films were removed, dried, and joined face-to-face with a "lid" section laser cut from the same film. The joined lid and substrate were dried in vacuum, and then thermally crosslinked at 80 °C for 8 additional hr to seal top and bottom layers (Fig. 1d iii). Surface-mount components were attached using low-temperature indium (In) solder and a hot air soldering gun for both unencapsulated and encapsulated boards (Fig. 1d iv).

The sheet resistance of deposited traces composed of Cr/Au and Ti/Au at 0.3 mVwas measured as 1.05 and 0.6 Ω·cm^{-2}, respectively (Fig. 4a i). For comparison, the theoretical ideal resistance of 5 nm of Ti and 95 nm Au is ~0.2 Ω·cm^{-2}. To characterize trace performance in the context of conventional AC operation (e.g. digital interfaces) or more advanced applications such as acoustic power transfer, AC impedance was investigated for traces deposited by physical vapor deposition on 0–48 films (Fig. 4a ii). Impedance magnitude and phase were monitored as a function of frequency across a range from 1 Hz to 5 MHz. Impedance magnitude remained constant across the frequency range, while a phase increase was observed beginning at 100 kHz. Traces consisting of Cr/Au layers showed a higher phase and magnitude compared to the Ti/Au traces (Fig. 4a ii). Electrical crosstalk (capacitive and/or inductive transfer of a signal between an active trace and an adjacent inactive trace) in small devices can lead to issues with signal integrity and device performance[88]. While crosstalk can be arbitrarily minimized by increasing inter-trace spacing, such a strategy is often nonideal in the context of implantable devices, where minimal device size is an important design goal. For single ended systems, a commonly used target amplitude of signal transfer between an active trace and an inactive neighboring trace is <−26 dB, or 5% of total signal

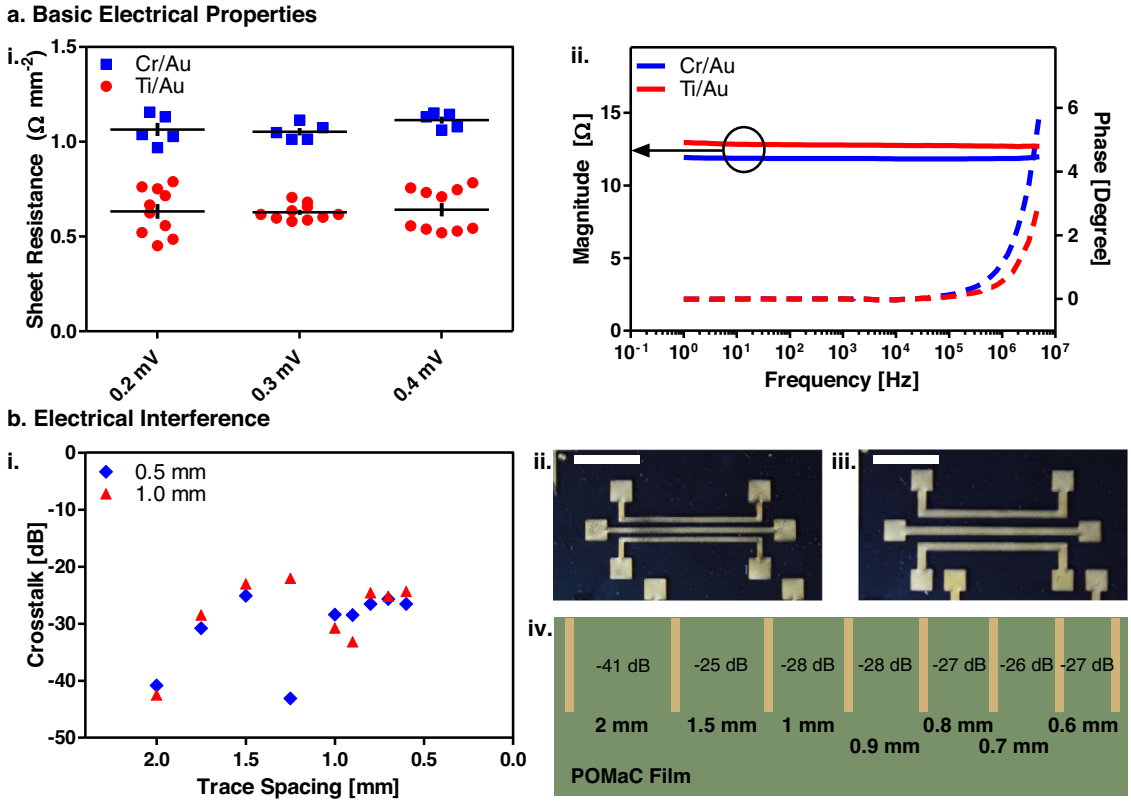

Fig. 4 Electrical characterizations. a Basic electrical properties. i. Sheet resistance for Cr/Au and Ti/Au traces on POMaC substrate. ii. Impedance characterization for Cr/Au and Ti/Au traces on POMaC substrate. **b** Crosstalk Properties. i. Crosstalk analysis reported in decibel loss for trace spacings between 2.0–0.6 mm for 0.5 mm and 1 mm trace widths for Ti/Au traces on POMaC substrates. ii. and iii. Configuration examples of the 0.5 mm and 1 mm trace widths, respectively, on POMaC substrates. iv. Representative dB losses for 0.5 mm trace widths at different spacings are also represented visually. Scale Bars = 10 mm. Error bars depict standard error of the mean.

of the active trace. Electrical crosstalk between Ti/Au traces deposited on POMaC was found to be ~−25 dB for inter-trace spacings between 2.0–0.6 mm when applying a 5 MHz signal to the active trace and monitoring the signal amplitude of the adjacent inactive trace (Fig. 4b i). Examples of circuit designs with different spacings are shown for 0.5 mm (Fig. 4b ii) and 1 mm (Fig. 4b iii) trace widths. As expected, increasing spacing between traces resulted in less observed crosstalk, and a graphical depiction of trace spacing and observed crosstalk for 0.5-mm-wide traces is included in Fig. 4b iv. Trace width did not change observed crosstalk between traces at the inter-trace spacings examined. Based on observed crosstalk, devices employing equivalent fabrication methods could expect to utilize inter-trace spacings as low as 0.6 mm, for signal bandwidths below 5 MHz. For the shadow mask materials used in this work, 0.6 mm was the resolution limit for long traces, so smaller inter-trace spacings may be possible when conventional photolithographic techniques or metal shadow masks, or in devices with even lower bandwidth requirements.

Electrical continuity under strain. Au traces exhibit strain resistance when deposited on an elastomeric substrate[35–37]. Such films are more durable when supported by a Cr[89] or Ti[90] adhesion layer, which prevents delamination. Aside from material selection, deterministic structures or designs that use geometry to allow for stretching in specific directions while minimizing local strains have also been used to increase the strain functionality of conductive traces[91]. In-plane structures typically involve a serpentine geometry with a horseshoe shape, which consists of meandering patterns that distribute stress across bends in the metal trace[92]. The resistance during cyclic tensile strain was monitored from 0–20% strain and used to calculate R/R_0. Results are shown in Fig. 5. Overall, these tests show that as strain is increased up to 20% the resistance of the traces increase, however limited hysteresis was observed after the first cycle. The POMaC material alone (without deposited electrodes) showed stable TM over repeated stress-strain cycles (Supplementary Fig. 4). For unencapsulated traces (Fig. 5a i and ii), R/R_0 increased with increasing strain and peaked at 20% strain with $R/R_0 = 40$, 41, 44, and 52 after cycles 1, 10, 100, and 1000, respectively. Increased cycling from first to 1000th strain cycle resulted in R/R_0 increase of ~30%. Additionally, similar baseline 0% strain values were observed across all cycles indicating that the initial resistance values are recoverable after repeated strain cycles. Encapsulated traces (Fig. 5b i and ii) showed a more rapid increase in R/R_0 with increasing strain. The R/R_0 values peaked at 20% strain with $R/R_0 = 41$, 47, 54, and 87 after cycles 1, 10, 100, and 1000, respectively. Increased cycling from the first to 1000th strain cycle resulted in R/R_0 increase of ~110%. The encapsulated traces were also resistant to changes with increasing cycle number and showed similar recovery of baseline 0% strain. Representative images of traces at up to 50% strain (Fig. 5a iii, B iii) show trace broadening with increasing strain for unencapsulated traces while encapsulated traces retain their original shapes and tend to fracture more rigidly. The difference in fracture patterns between the examined traces could explain the more rapid increase in R/R_0 observed for encapsulated traces. The encapsulated traces develop larger and spatially separated cracks, likely due to the bonding of top and bottom layers, instead of broadening with many localized cracks like unencapsulated traces. Detailed graphs of strain resistance data are included in the supplementary information (Supplementary Figs. 2–5).

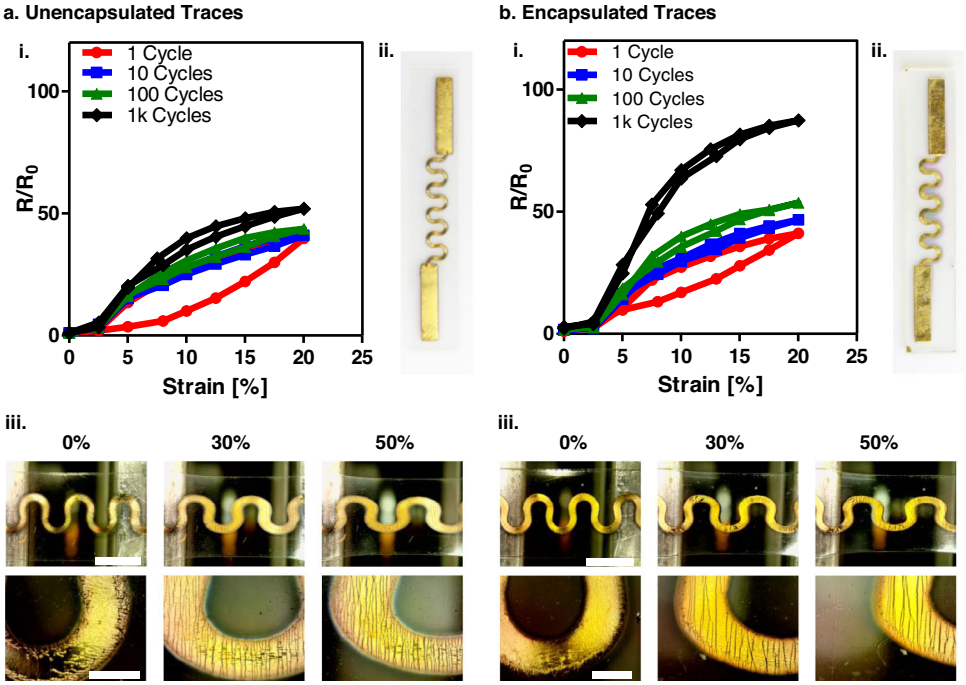

Fig. 5 Response of serpentine POMaC traces to strain. a Unencapsulated Traces. i. R/R_0 graphs for unencapsulated traces from 0 to 20% strain over 1000 cycles ($R_0 = 108 \pm 10\ \Omega$) ($n = 6$). ii. Image of unencapsulated POMaC circuit. **iii**. Photographs of unencapsulated POMaC circuit at 0, 30, and 50% strains. Scale Bars = 3.3 mm (top row), 200 µm (bottom row). **b** Encapsulated Traces. i. R/R_0 graphs for encapsulated traces from 0 to 20% strain over 1000 cycles ($R_0 = 93 \pm 5\ \Omega$) ($n = 7$). **ii**. Image of encapsulated POMaC circuit. **iii**. Photographs of unencapsulated POMaC circuit at 0, 30, and 50% strain. Scale Bars = 3.3 mm (top row), 200 µm (bottom row).

Applications

POMaC circuit boards exhibit elastomeric properties and have potential in a variety of applications. Figure 6a shows POMaC circuit boards being bent, twisted, and stretched. An LED circuit on a POMaC circuit board was demonstrated in operation during tensile strain (Fig. 6b). To demonstrate the usefulness of POMaC substrates in applications where surface functionalization is required, the surface of POMaC circuits were chemically patterned (Fig. 6c). In this case, the backbone carbon-carbon double bond groups were utilized to link thiol-functionalized fluorescein isothiocyanate (FITC) to the film surface. Using similar approaches, it is possible to conjugate other biomaterials, e.g., peptides, growth factors, and aptamers, to develop bio-integrated circuits using the same backbone groups or bond functional materials for advanced packaging applications, e.g., adhesives, anti-fouling coatings, etc. Encapsulated POMaC LED circuits were fabricated and demonstrated in simulated in vivo conditions (Fig. 6d). The circuit was fabricated and encapsulated in a second POMaC layer, and metallic pads were covered and sealed using photocrosslinked P6 prior to operation in simulated physiological conditions. Under these conditions, the LED circuit operated continuously for 8 h. Failure occurred due to swelling and eventual delamination of the POMaC sealant over the contact pads of the surface-mount LED (Fig. 6d). In the future, sealant layers could receive additional thermal crosslinking to provide increased swelling resistance. To demonstrate the potential for increased circuit complexity, a comparator type circuit was constructed on the POMaC circuit board. Figure 7 shows photographs of the board in operation (Fig. 7a–c) along with electrical characterization of the circuit in operation with different frequency input signals (Fig. 7d). These POMaC-based elastomeric circuit boards can be tuned based on crosslinking conditions to a variety of target physical properties including degradation rate and tensile modulus which can enable tailoring of these circuit substrates to specific applications. Future work will continue to develop microfabrication processes for POMaC-based elastomer circuit boards and explore the engineering of advanced circuits and microsystems with POMaC-based packaging.

METHODS

Materials

1,8-octane diol (OD), maleic anhydride (MA), citric acid (CA), 2-Hydroxy-4′-(2-hydroxyethoxy)-2-methylpropiophenone (Irgacure 2959), 1,4-dioxane, dimethyl sulfoxide-d6, were purchased from Millipore Sigma (Burlington, MA). Dextran with average M.W. 500 kDa and 4′,6-diamidino-2-phenylindole (DAPI) were sourced from ThermoFisher Scientific (Waltham, MA). Silicon wafers were purchased from University Wafer (South Boston, MA). Indium solder (Indalloy® #290) was procured from Indium Corporation (Clinton, NY). Surface-mount resistors (ERJ-8GEYJ680V) and LEDs (LTST-C230KRKT) were obtained from Digi-Key (Thief River Falls, MN). Fluorescein-polyethylene glycol-thiol (FITC-PEG-SH) 1k MW was purchased from Creative PEGWorks (Chapel Hill, NC).

POMaC pre-polymer synthesis

Pre-polymer synthesis was performed based on procedures adapted from Tran et al.[63] using a melt poly-condensation reaction. Citric acid (CA), maleic anhydride (MA), and 1,8-octanediol (OD) monomers were placed in a moisture-free 500 mL three-necked round bottom flask under nitrogen atmosphere. Initial melting was performed at 160 °C using a temperature-controlled silicone oil bath and stirring. The temperature of the melt system was then lowered to 140 °C and purged under nitrogen for 5 h. Three pre-polymers were synthesized for initial investigation by varying the ratio of citric acid to maleic anhydride and maintaining the ratio of diols to acids: *(i)* pre-POMaC 4 (MA/CA/OD: 2/3/5), *(ii)* pre-POMaC 6 (MA/CA/OD: 3/2/5), and *(iii)* pre-POMaC 8 (MA/CA/OD: 4/1/5). To remove unreacted monomers and short polymer

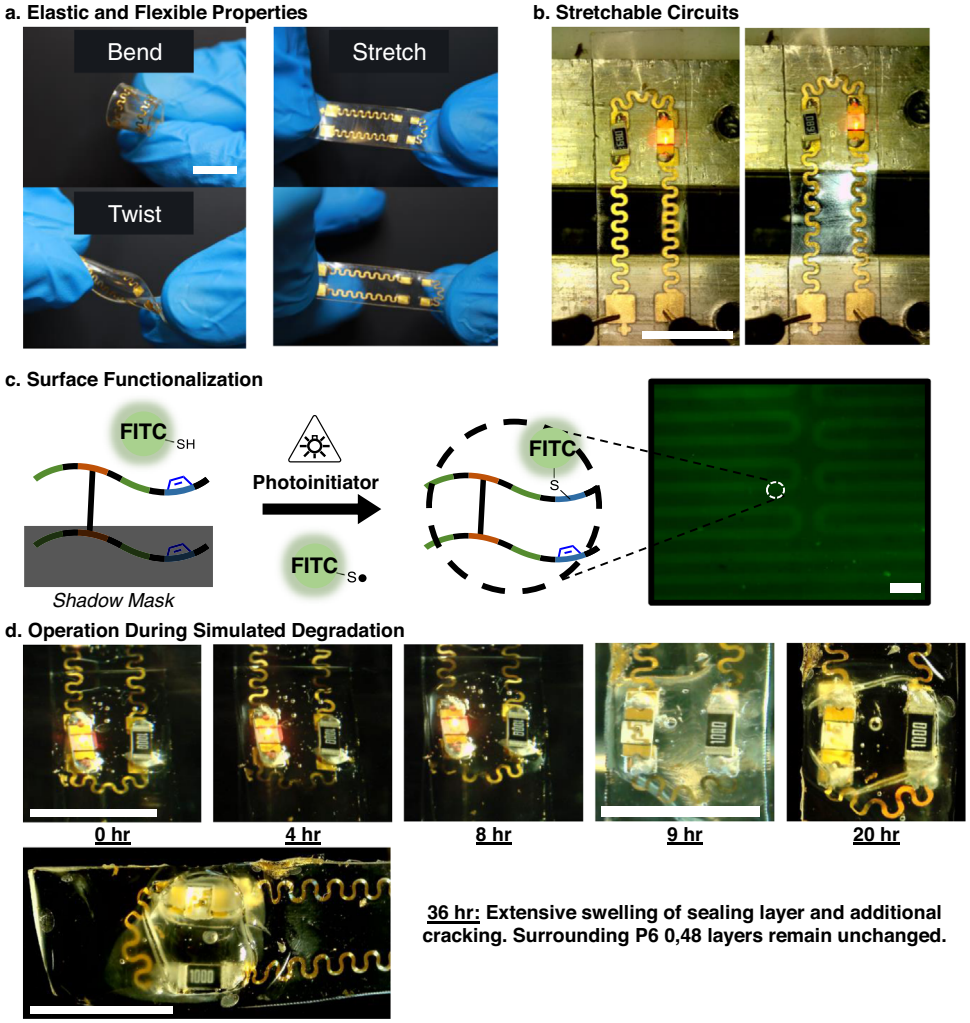

Fig. 6 Application examples for POMaC circuits. a POMaC circuit boards exhibit elastic properties and can be bent, twisted, and stretched (scale bar: 9 mm). **b** Fully functional LED circuit with POMaC circuit board being operated during tensile strain (scale bar: 9 mm). **c** Micrograph of POMaC circuit board surface patterned with fluorescent dye by photocrosslinking. Scale Bar = 500 μm. **d** Encapsulated POMaC circuit board operating in simulated biofluid. Scale Bar = 9 mm.

chains, each reaction mixture was dissolved in minimal dioxane and dropwise precipitated in deionized water (1 L) twice. After dropwise purification, pre-polymer was mixed by vortex with equal volume of water, frozen at −80 °C overnight, and lyophilized for 48 h. For films receiving photo crosslinking, 5% w/w Irgacure 2959:pre-polymer was added.

Pre-polymer characterization

All pre-polymer synthesis reactions were conducted for 5 h with periodic sampling. To identify monomer molar ratios at specific time points, the collected samples were dissolved at 10 mg mL^{-1} in dimethyl sulfoxide-d6 (d6-DMSO) and analyzed by ^{1}H-NMR using an AvanceNeo 400 MHz (Bruker, Billerica, MA). Chemical shifts were identified based on relative reference to tetramethylsilane (TMS, 0.00 ppm). Thermal degradation characteristics for each final pre-polymer were obtained by thermogravimetric analysis with temperature ramp to 600 °C at 10 °C min^{-1} under nitrogen using a SDT 650 (TA Instruments, New Castle, DE).

Thin film fabrication

Thin pre-polymer films composed of POMaC 6 (P6) pre-polymer containing 5% w/w Irgacure 2959 with respect to total P6 pre-polymer weight were deposited on silicon wafers by spin coating using a WS-650 spin coater (Laurell, North Wales, PA). Silicon wafers were cleaned by sonication in DI water, acetone, and isopropyl alcohol. Silicon wafers were then surface treated with plasma for 2 min in a PDC-001 plasma cleaner (Harrick Plasma, Ithaca, NY). A 20% w/w solution of dextran in MilliQ water was then applied as a sacrificial layer to enable simple lift-off. The dextran solution was applied to cover 90% of the wafer area, spun at 2000 RPM for 15 s, and crystalized on a hot plate at 150 °C for 2 min[93]. After sacrificial layer deposition, the P6 pre-polymer was applied (5 ×800 μL) at the center of the wafer and spread by spin coating as detailed in Table 3. The coated wafers were then photocrosslinked using a Model 2000AF Exposure System (OAI, Milpitas, CA) followed by thermal crosslinking at 80 °C to produce crosslinked films (see Table 2 for photo and thermal crosslinking for each condition). Figure 1d shows a representation of the film fabrication method. The thickness of films was evaluated using a Carbide IP65 Electronic Outside Micrometer (Mitutoyo, Kawasaki, Japan) at five separate locations on the film surface. Throughout experimentation, film thickness with the listed spin parameters varied based on POMaC batch. It is suspected that earlier batches of POMaC pre-polymer contained higher amounts of residual dioxane, which led to thinner films. We expect that addition of a casting agent

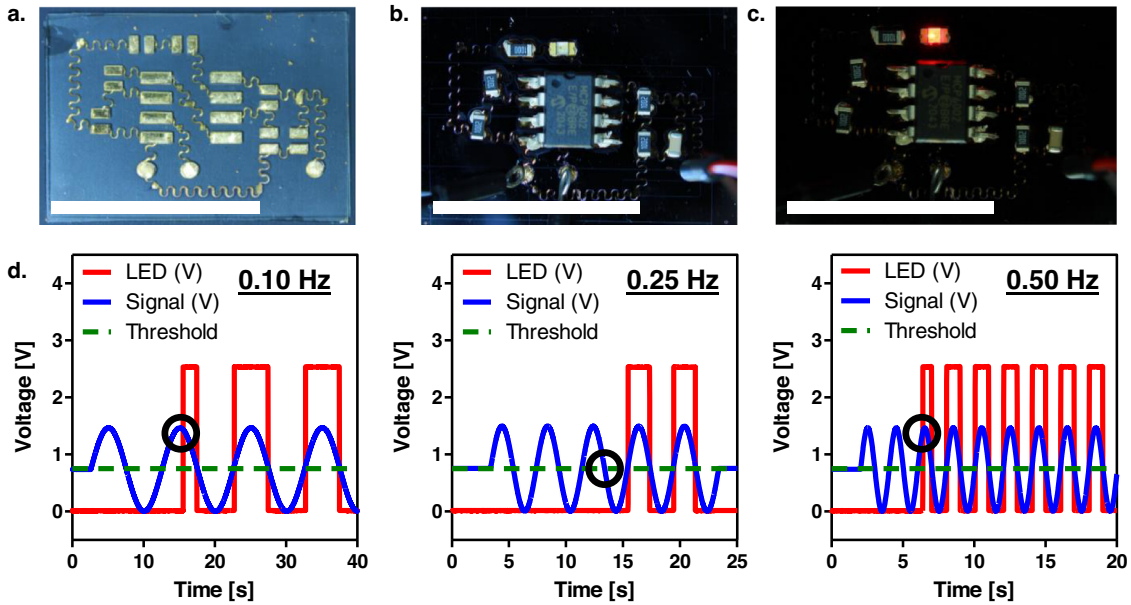

Fig. 7 Example comparator POMaC circuit. a POMaC circuit boards can be designed with multiple component attachment locations. **b** Fully functional POMaC circuit board implementing a comparator circuit. The LED is not illuminated when the applied sinusoidal input signal (+0.75 V magnitude, +0.75 V offset) is less than the applied threshold signal (+0.75 V), due to an amplifier output of 0 V. **c** When the input signal surpasses the threshold signal, the amplifier output increases and the LED is illuminated. **d** Voltage monitoring of the circuit in operation with various frequencies of input signal (0.1, 0.25, and 0.5 Hz). For each frequency, the black circle represents the time at which the amplifier receives power. Once the amplifier is powered and the threshold voltage is surpassed, the LED is forward-biased by the positive amplifier output voltage. Note that total LED illumination time for each cycle decreases as the frequency of input signal is increased (due to a shorter cycle period). Scale Bar = 26 mm.

(e.g., dioxane) to POMaC pre-polymer would enable controlled film thickness, but merely increasing spread or spin phase RPM, acceleration, or time did not allow for film thickness control. The films were then laser cut to produce individual samples using a custom XLS laser cutter (Universal Laser Systems, Scottsdale, AZ). The films were immersed in DI water for lift-off.

Swelling characterization

The sol content ($n \geq 24$) and swelling ratios ($n \geq 6$) of P6 films prepared with different crosslinking conditions were determined by mass differential. Laser cut films were air dried, weighed (w_i), and placed in DMSO for 3 days with solvent changes every 24 h; the films were then weighed (w_s), placed in DI water for 24 h to leach DMSO, and lyophilized for 72 h; the films were finally weighed to obtain dry weights (w_d). Sol content was calculated using Eq. (1). Swelling was calculated using Eq. (2).

$$(w_i - w_d)/w_i * 100\% \quad (1)$$

$$(w_s - w_d)/w_d * 100\% \quad (2)$$

Swelling kinetics

The swelling kinetics of 0–48 P6 films were determined by mass differential. Laser cut films (diameter 22 mm) were immersed in either PBS or DI water at either room temperature or 37 °C. The films were periodically weighed (w_t) over 24 h. At the final time point, the samples were rinsed with DI water, frozen and lyophilized to obtain final dry weight (w_d). The measured weights were converted into mass swelling percent using Eq. (3).

$$(w_t - w_d)/w_i * 100\% \quad (3)$$

In vitro degradation

Accelerated degradation was performed in 0.05 M NaOH to compare the relative degradation rates between P6 curing conditions. Laser cut films were lyophilized, weighed ($w_{initial}$), and placed in 0.05 M NaOH (2 mL) at room temperature. Samples ($n = 4$) were removed from NaOH at different time points, washed in DI water overnight, lyophilized, and weighed (w_{final}). The remaining samples received fresh NaOH at each time point. The mass loss percentage was calculated by Eq. (4).

Long term in vitro degradation

Similarly, prepared samples of 0–48 P6 films were used to examine long term degradation behaviors in DI water and PBS. The samples were weighed ($w_{initial}$), placed in 2 mL of the specified solution, and monitored over 10 weeks at 37 °C. At each timepoint ($n = 4$), samples were rinsed with DI water, blotted dry, weighed (w_{swell}), lyophilized, and then reweighed (w_{final}). Equations (4) and (5) were used to calculate the mass loss and swelling loss at each time point, respectively.

$$(w_{initial} - w_{final})/w_{initial} \times 100\% \quad (4)$$

$$(w_{swell} - w_{final})/w_{initial} \times 100\% \quad (5)$$

Mechanical characterization

The mechanical properties of P6 films for each curing condition ($n \geq 4$) were characterized using a Discovery HR-30 (TA Instruments, New Castle, DE) in tension fixture mode. POMaC films were laser cut into 12.7 × 30 mm^2 rectangles, removed from wafer, and dried. The samples were then elongated at 15 µm s^{-1} while monitoring force and displacement. The initial tensile modulus was derived from the resulting stress-strain curves within the 1–5% strain window; tensile strength and elongation at break were also recorded.

Table 3. POMaC pre-polymer spin coating settings and resulting film thickness.

Spread Stage			Spin Stage			Thickness (μm)
RPM	Acc.	Time (s)	RPM	Acc.	Time (s)	
750	172	15	850	172	10	412 ± 13

Thickness reported as mean ± standard error of the mean.
RPM revolutions per minute, *Acc.* acceleration, *s* seconds.

POMaC-ECB fabrication

0–48 P6 films were used to create elastic circuit boards. Shadow masks of paper were designed for each circuit in AutoCAD and laser cut. The masks were attached to POMaC films, then a titanium or chromium adhesion layer (thickness: 5 nm) and a gold conductive layer (thickness: 95 nm) were sequentially deposited by sputtering using a PVD 75 physical vapor deposition system (Kurt J. Lesker Company, Jefferson Hills, PA); all depositions were conducted at chamber pressures less than 4×10^{-5} torr. After deposition, films were laser cut, immersed in DI water to dissolve dextran, and POMaC circuits were removed from the wafer substrate using gentle lifting with tweezers. To demonstrate encapsulated electrical circuits, 0–48 POMaC circuits were prepared as described above but cured for only 40 h prior to metal deposition. POMaC substrates, with metallized traces, and POMaC encapsulation layers were laser cut, removed from the carrier wafer, dried, aligned, vacuum dried, and thermally cross-linked at 80 °C for 8 additional hr to create sealed circuit boards with openings for contact pads.

Electrical characterization

The stability of the horseshoe style traces on 0–48 P6 films was examined by comparison of direct current (DC) resistance before and after film removal using a B2902A SMU (Keysight, Colorado Springs, CO). The resistance was measured by applying a 100 μA current with 2.1 V compliance on replicate samples ($n \geq 8$).

Sheet resistance

POMaC circuits with a 15 mm × 15 mm square of deposited Ti (5 nm) and Au (95 nm) layers were next investigated for the sheet resistance of deposited metal layers using a 4-point probe. To avoid artifacts generated by deformation of the conductive film under pressure from a standard probe head, an alternative contact strategy was employed in which electrical contact with the conductive film was established using silver epoxy applied and cured in situ. First, a polydimethylsiloxane (PDMS, Sylgard 184, 9:1 base:curing agent ratio) spacer with four equally separated cavities (1 mm^2 by 2 mm depth, 1.54 mm spacing) was cast using a 3D-printed mold (Formlabs). Cast PDMS spacers were placed on top of the POMAC-metal film samples, and conductive epoxy (8331S, MG Chemicals) was used to fill each cavity. Prior to curing, the top surface of the PDMS spacer was cleaned to eliminate any epoxy bridging between adjacent cavities, and bent wire leads were inserted into each volume of epoxy to serve as test connections. A Keysight B2902A SMU was used to deliver between 0.2–0.4 mA and resistance monitored ($n > 5$ for each current level). A correction factor (0.9313) was applied to calculate the actual sheet resistance[94,95].

Trace impedance

Trace impedance was characterized using a combination function generator-oscilloscope (Analog Discovery 2, Digilent). Sputtered conductive traces (pads: 5 × 5 mm^2, trace width: 1 mm, trace length: 25 mm, total thickness: 100 nm) were connected to short sections of 20ga. single-stranded wire using silver conductive epoxy (8330S, MG Chemicals, 1 h cure at 80 °C) to facilitate connection to test equipment. A sinusoidal excitation waveform (2 V peak-to-peak, 0 V DC offset) was applied to each trace in series with a 10.06 Ω reference resistor, and the resulting voltage drop across the trace and current signal phase shift were measured to determine impedance. The excitation frequency was varied over a 1 Hz–5 MHz range in 68 steps (10 steps per decade), with each impedance measurement averaged over 1 s.

Trace crosstalk

Crosstalk was measured by applying a sinusoidal potential to an active "transmitter" trace and measuring the observed response at an inactive, non-driven "receiver" trace deposited on the same substrate. Multiple transmitter-receiver trace pairs with varying trace width (0.5 mm and 1 mm) and spacing (0.5–2 mm) were tested to evaluate the effect of trace separation on severity of crosstalk. Traces were epoxied (8331S, MG Chemicals) to sections of wire as previously described. Using a combination function generator-oscilloscope (Analog Discovery 2, Digilent) a 5 MHz sine wave (2 V peak-to-peak, 0 V DC offset) was applied across the transmitter trace, and both the input sine wave and the transferred signal at the adjacent receiver trace were simultaneously measured. To compensate for source loading, the received signal was normalized to the simultaneously measured input signal. This procedure was repeated for each transmitter-receiver pair across all tested substrates.

Strain resistance

The strain resistance of POMaC circuit boards, unencapsulated ($n = 6$) and encapsulated ($n = 7$), were examined by connecting samples with horseshoe style traces ($\theta = 113°$ $r = 0.8$ mm and width = 0.2 mm) onto a MDrive linear actuator (Schneider Electric, Hartford, CT) and measuring resistance using a B2902A SMU (Keysight, Colorado Springs, CO) while stretching the films to predetermined strains ranging from 0 to 20%. The films were stretched from 0 to 20% for up to 1000 cycles and resistance monitored during the 1st, 10th, 100th, and 1000th cycle.

Assembly with surface-mount devices

POMaC circuit boards were fabricated as described above and patterned to assemble a simple LED circuit, a modified multilayer LED circuit, and a comparator circuit. After drying of the metallized POMaC films, surface-mount devices were soldered to the POMaC circuit boards with low-temperature indium solder (Indium Corporation, Clinton, NY) and hot air processing. This combination of solder and processing technique were selected because the higher temperatures associated with conventional reflow conditions resulted in damage to POMaC films.

Construction and demonstration of encapsulated circuit board

A modified 2-layer design was demonstrated using POMaC for substrate, encapsulating layers, and sealant for pad contacts. P6 films were prepared as described above, but received only 40 h of thermal crosslinking (P6 0–40 films) before metallization. After metallization, substrate and encapsulant layers were laser cut from the same film (Fig. 1d ii). The encapsulation and substrate layers were dried in vacuum, aligned (face to face), dried again to remove moisture, and finally thermally crosslinked for an additional 8 h at 80 °C (Fig. 1d iii). After the final thermal crosslinking, surface-mount resistors and LEDs were attached to the contact pads using indium solder (Fig. 1d iv). To seal the contact pads and surface-mount components, P6 pre-polymer with 5% w/w Irgacure 2959 and 5% w/w dithiothreitol was applied over the attached components and open pads and then

photocrosslinked (30 mJ·cm^{-2} for 5 min). After sealing, the board was submerged in PBS and monitored over time.

Photopatterning

To demonstrate the potential for biopatterning of POMaC films, 0–48 P6 films were incubated in a PBS solution containing 0.5 mg·mL^{-1} FITC-PEG-SH and 1% w/w PI for 0, 0.5, 1, and 3 h. A shadow mask was applied to each film and UV dose of 1.2·J cm^{-2} was delivered through the shadow mask using the DYMAX BlueWave AX-550 and RediCure UV curing system (Torrington, CT). The films were then washed in PBS for 5 days and imaged using a fluorescent microscope under identical conditions. Control films were prepared in the same manner using solutions lacking either FITC or PI.

Statistical methods

When determining linearity, the Runs test ($P < 0.05$) was used. To compare physical properties between crosslinking conditions 1-way ANOVA with a Turkey test ($P < 0.05$) was used to determine significance.

DATA AVAILABILITY

The data that substantiate the findings of this study are available from the corresponding author upon reasonable request.

Received: 9 August 2022; Accepted: 15 May 2023;
Published online: 01 June 2023

REFERENCES

1. Hazra, A. et al. in *Waste valorisation and recycling*. 203–217 (Springer, 2019).
2. Islam, A. et al. Advances in sustainable approaches to recover metals from e-waste-A review. *J. Clean. Prod.* **244**, 118815 (2020).
3. Li, W. et al. Biodegradable materials and green processing for green electronics. *Adv. Mater.* **32**, 2001591 (2020).
4. Li, C. et al. Design of biodegradable, implantable devices towards clinical translation. *Nat. Rev. Mater.* **5**, 61–81 (2020).
5. Li, R., Wang, L., Kong, D. & Yin, L. Recent progress on biodegradable materials and transient electronics. *Bioact. Mater.* **3**, 322–333 (2018).
6. Lee, W. H., Cha, G. D. & Kim, D.-H. Flexible and biodegradable electronic implants for diagnosis and treatment of brain diseases. *Curr. Opin. Biotechnol.* **72**, 13–21 (2021).
7. Liu, J. et al. Future paper based printed circuit boards for green electronics: fabrication and life cycle assessment. *Energy Environ. Sci.* **7**, 3674–3682 (2014).
8. Lin, Y., Gritsenko, D., Liu, Q., Lu, X. & Xu, J. Recent advancements in functionalized paper-based electronics. *ACS Appl. Mater. Interfaces* **8**, 20501–20515 (2016).
9. Manam, N. et al. Study of corrosion in biocompatible metals for implants: a review. *J. Alloys Compd.* **701**, 698–715 (2017).
10. Shim, J.-S., Rogers, J. A. & Kang, S.-K. Physically transient electronic materials and devices. *Mater. Sci. Eng. R Rep.* **145**, 100624 (2021).
11. Zhang, F. & King, M. W. Biodegradable polymers as the pivotal player in the design of tissue engineering scaffolds. *Adv. Healthc. Mater.* **9**, 1901358 (2020).
12. Asghari, F., Samiei, M., Adibkia, K., Akbarzadeh, A. & Davaran, S. Biodegradable and biocompatible polymers for tissue engineering application: a review. *Artif. Cells Nanomed. Biotechnol.* **45**, 185–192 (2017).
13. Qiu, M. et al. Biocompatible and biodegradable inorganic nanostructures for nanomedicine: silicon and black phosphorus. *Nano Today* **25**, 135–155 (2019).
14. Lu, L. et al. Biodegradable monocrystalline silicon photovoltaic microcells as power supplies for transient biomedical implants. *Adv. Energy Mater.* **8**, 1703035 (2018).
15. Tan, Y. J. et al. A transparent, self-healing and high-κ dielectric for low-field-emission stretchable optoelectronics. *Nat. Mater.* **19**, 182–188 (2020).
16. Wang, C., Wang, C., Huang, Z. & Xu, S. Materials and structures toward soft electronics. *Adv. Mater.* **30**, 1801368 (2018).
17. Llerena Zambrano, B. et al. Soft electronics based on stretchable and conductive nanocomposites for biomedical applications. *Adv. Healthc. Mater.* **10**, 2001397 (2021).
18. Rao, Z. et al. Soft electronics for the skin: from health monitors to human–machine interfaces. *Adv. Mater. Technol.* **5**, 2000233 (2020).
19. Ray, T. R. et al. Bio-integrated wearable systems: a comprehensive review. *Chem. Rev.* **119**, 5461–5533 (2019).
20. Kang, J., Tok, J. B.-H. & Bao, Z. Self-healing soft electronics. *Nat. Electron.* **2**, 144–150 (2019).
21. Zhou, Y. et al. Highly stretchable, elastic, and ionic conductive hydrogel for artificial soft electronics. *Adv. Funct. Mater.* **29**, 1806220 (2019).
22. Wu, W. Stretchable electronics: functional materials, fabrication strategies and applications. *Sci. Technol. Adv. Mater.* **20**, 187–224 (2019).
23. Hong, Y. J., Jeong, H., Cho, K. W., Lu, N. & Kim, D. H. Wearable and implantable devices for cardiovascular healthcare: from monitoring to therapy based on flexible and stretchable electronics. *Adv. Funct. Mater.* **29**, 1808247 (2019).
24. Han, H. et al. Trends in epidermal stretchable electronics for noninvasive long-term healthcare applications. *Int. J. Autom. Smart Technol.* **7**, 37–52 (2017).
25. Liu, Y., Pharr, M. & Salvatore, G. A. Lab-on-skin: a review of flexible and stretchable electronics for wearable health monitoring. *ACS Nano* **11**, 9614–9635 (2017).
26. Vallem, V., Sargolzaeiaval, Y., Ozturk, M., Lai, Y. C. & Dickey, M. D. Energy harvesting and storage with soft and stretchable materials. *Adv. Mater.* **33**, 2004832 (2021).
27. Alici, G. Softer is harder: what differentiates soft robotics from hard robotics? *MRS Adv.* **3**, 1557–1568 (2018).
28. Cianchetti, M., Laschi, C., Menciassi, A. & Dario, P. Biomedical applications of soft robotics. *Nat. Rev. Mater.* **3**, 143–153 (2018).
29. Hartmann, F., Baumgartner, M. & Kaltenbrunner, M. Becoming sustainable, the new frontier in soft robotics. *Adv. Mater.* **33**, 2004413 (2021).
30. Liu, K., Tran, H., Feig, V. R. & Bao, Z. Biodegradable and stretchable polymeric materials for transient electronic devices. *MRS Bull.* **45**, 96–102 (2020).
31. Chatterjee, S., Saxena, M., Padmanabhan, D., Jayachandra, M. & Pandya, H. J. Futuristic medical implants using bioresorbable materials and devices. *Biosensors Bioelectron.* **142**, 111489 (2019).
32. Moon, D.-B., Lee, J., Roh, E. & Lee, N.-E. Three-dimensional out-of-plane geometric engineering of thin films for stretchable electronics: a brief review. *Thin Solid Films* **688**, 137435 (2019).
33. Pan, T. et al. Experimental and theoretical studies of serpentine interconnects on ultrathin elastomers for stretchable electronics. *Adv. Funct. Mater.* **27**, 1702589 (2017).
34. Rogers, J. A., Someya, T. & Huang, Y. Materials and mechanics for stretchable electronics. *Science* **327**, 1603–1607 (2010).
35. Lacour, S. P., Chan, D., Wagner, S., Li, T. & Suo, Z. Mechanisms of reversible stretchability of thin metal films on elastomeric substrates. *Appl. Phys. Lett.* **88**, 204103 (2006).
36. Lacour, S. P., Jones, J., Wagner, S., Li, T. & Suo, Z. Stretchable interconnects for elastic electronic surfaces. *Proc. IEEE* **93**, 1459–1467 (2005).
37. Graz, I. M., Cotton, D. P. & Lacour, S. P. Extended cyclic uniaxial loading of stretchable gold thin-films on elastomeric substrates. *Appl. Phys. Lett.* **94**, 071902 (2009).
38. Matsuhisa, N. et al. Printable elastic conductors by in situ formation of silver nanoparticles from silver flakes. *Nat. Mater* **16**, 834–840 (2017).
39. Xu, J. et al. Highly stretchable polymer semiconductor films through the nanoconfinement effect. *Science* **355**, 59–64 (2017).
40. Cuttaz, E. et al. Conductive elastomer composites for fully polymeric, flexible bioelectronics. *Biomater. Sci.* **7**, 1372–1385 (2019).
41. Ye, H., Zhang, K., Kai, D., Li, Z. & Loh, X. J. Polyester elastomers for soft tissue engineering. *Chem. Soc. Rev.* **47**, 4545–4580 (2018).
42. Wang, R. et al. A highly stretchable and transparent silver nanowire/thermoplastic polyurethane film strain sensor for human motion monitoring. *Inorg. Chem. Front.* **6**, 3119–3124 (2019).
43. Chen, S. et al. in *2017 IEEE 19th Electronics Packaging Technology Conference (EPTC)*, 1–4 (IEEE, 2017).
44. Ning, N. et al. Highly stretchable liquid metal/polyurethane sponge conductors with excellent electrical conductivity stability and good mechanical properties. *Compos. B. Eng.* **179**, 107492 (2019).
45. Lim, T., Kim, H. J., Zhang, H. & Lee, S. Screen-printed conductive pattern on spandex for stretchable electronic textiles. *Smart Mater. Struct.* **30**, 075006 (2021).
46. Lopes, P. A. et al. Soft bioelectronic stickers: selection and evaluation of skin-interfacing electrodes. *Adv. Healthc. Mater.* **8**, 1900234 (2019).
47. Chen, X. et al. Stretchable supercapacitors as emergent energy storage units for health monitoring bioelectronics. *Adv. Energy Mater.* **10**, 1902769 (2020).
48. Kim, T., Yi, Q., Hoang, E. & Esfandyarpour, R. A 3D Printed Wearable Bioelectronic Patch for Multi-Sensing and In Situ Sweat Electrolyte Monitoring. *Adv. Mater. Technol.* **6**, 2001021 (2021).
49. Sim, K. et al. An epicardial bioelectronic patch made from soft rubbery materials and capable of spatiotemporal mapping of electrophysiological activity. *Nat. Electron.* **3**, 775–784 (2020).

50. Li, G. et al. PEDOT: PSS/grafted-PDMS electrodes for fully organic and intrinsically stretchable skin-like electronics. *ACS Appl. Mater. Interfaces* **11**, 10373–10379 (2019).
51. Salihu, R. et al. Citric acid: a green cross-linker of biomaterials for biomedical applications. *Eur. Polym. J.* **146**, 110271 (2021).
52. Koper, F. et al. Advancements in structure–property correlation studies of cross-linked citric acid-based elastomers from the perspective of medical application. *J. Mater. Chem. B* **9**, 6425–6440 (2021).
53. Turner, B., Ramesh, S., Menegatti, S. & Daniele, M. Resorbable elastomers for implantable medical devices: highlights and applications. *Polym. Int*. **71**, 552–561 (2021).
54. Yang, J., Webb, A. R. & Ameer, G. A. Novel citric acid-based biodegradable elastomers for tissue engineering. *Adv. Mater.* **16**, 511–516 (2004).
55. Djordjevic, I., Choudhury, N. R., Dutta, N. K. & Kumar, S. Poly [octanediol-co-(citric acid)-co-(sebacic acid)] elastomers: novel bio-elastomers for tissue engineering. *Polym. Int.* **60**, 333–343 (2011).
56. Chon, Y. J. et al. Synthesis of a high-performance citric acid-based polyester elastomer by a hot-pressing technique. *Polymer* **125**, 283–291 (2017).
57. Thomas, L. V. & Nair, P. D. (Citric acid–co–polycaprolactone triol) polyester: a biodegradable elastomer for soft tissue engineering. *Biomatter* **1**, 81–90 (2011) .
58. Zou, F., Sun, X. & Wang, X. Elastic, hydrophilic and biodegradable poly (1, 8-octanediol-co-citric acid)/polylactic acid nanofibrous membranes for potential wound dressing applications. *Polym. Degrad. Stab.* **166**, 163–173 (2019).
59. Guo, Y., Liang, K. & Ji, Y. New degradable composite elastomers of POC/PCL fabricated via in-situ copolymerization blending strategy. *Eur. Polym. J.* **110**, 337–343 (2019).
60. Yang, J. et al. Modulating expanded polytetrafluoroethylene vascular graft host response via citric acid-based biodegradable elastomers. *Adv. Mater.* **18**, 1493–1498 (2006).
61. Liu, Y., Li, T., Han, Y., Li, F. & Liu, Y. Recent development of electrospun wound dressing. *Curr. Opin. Biomed. Eng.* **17**, 100247 (2021).
62. Jafari, F. et al. Development of an electrospun scaffold for retinal tissue engineering. *Polym. Sci. Ser. B* **62**, 290–298 (2020).
63. Tran, R. T. et al. Synthesis and characterization of a biodegradable elastomer featuring a dual crosslinking mechanism. *Soft Matter* **6**, 2449–2461 (2010).
64. Boutry, C. M., Schroeder, B. C., Bao, Z., Legrand, A. & Fox, P. in *IEEE Transactions Biomedical Circuits and Systems,* 144–147 (IEEE, 2016).
65. Boutry, C. M. et al. A stretchable and biodegradable strain and pressure sensor for orthopaedic application. *Nat. Electron.* **1**, 314–321 (2018).
66. Wang, Z. et al. Polymer network editing of elastomers for robust underwater adhesion and tough bonding to diverse surfaces. *ACS Appl. Mater. Interfaces* **13**, 36527–36537 (2021).
67. Boutry, C. M. et al. Biodegradable and flexible arterial-pulse sensor for the wireless monitoring of blood flow. *Nat. Biomed. Eng.* **3**, 47–57 (2019).
68. Davenport Huyer, L. et al. Highly elastic and moldable polyester biomaterial for cardiac tissue engineering applications. *ACS Biomater. Sci. Eng.* **2**, 780–788 (2016).
69. Montgomery, M. et al. Flexible shape-memory scaffold for minimally invasive delivery of functional tissues. *Nat. Mater* **16**, 1038–1046 (2017).
70. Zhang, B., Montgomery, M., Davenport-Huyer, L., Korolj, A. & Radisic, M. Platform technology for scalable assembly of instantaneously functional mosaic tissues. *Sci. Adv.* **1**, e1500423 (2015).
71. Zhang, B. et al. Microfabrication of AngioChip, a biodegradable polymer scaffold with microfluidic vasculature. *Nat. Protoc.* **13**, 1793–1813 (2018).
72. Zhang, B. et al. Biodegradable scaffold with built-in vasculature for organ-on-a-chip engineering and direct surgical anastomosis. *Nat. Mater* **15**, 669–678 (2016).
73. Wang, E. Y. et al. Biowire model of interstitial and focal cardiac fibrosis. *ACS Cent. Sci.* **5**, 1146–1158 (2019).
74. Zhao, Y. et al. A multimaterial microphysiological platform enabled by rapid casting of elastic microwires. *Adv. Healthc. Mater.* **8**, 1801187 (2019).
75. Sengupta, S. et al. Branched/hyperbranched copolyesters from poly (vinyl alcohol) and citric acid as delivery agents and tissue regeneration scaffolds. *Macromol. Chem. Phys.* **222**, 2100134 (2021).
76. Fu, K. K., Wang, Z., Dai, J., Carter, M. & Hu, L. Transient electronics: materials and devices. *Chem. Mater.* **28**, 3527–3539 (2016).
77. Kim, H. J., Reddi, Y., Cramer, C. J., Hillmyer, M. A. & Ellison, C. J. Readily degradable aromatic polyesters from salicylic acid. *ACS Macro Lett.* **9**, 96–102 (2020).
78. Xu, X.-J., Sy, J. C. & Shastri, V. P. Towards developing surface eroding poly (α-hydroxy acids). *Biomat.* **27**, 3021–3030 (2006).
79. Woodard, L. N. & Grunlan, M. A. Hydrolytic degradation and erosion of polyester biomaterials. *ACS Macro Lett.* **7**, 976–982 (2018).
80. Qi, D. et al. Highly stretchable, compliant, polymeric microelectrode arrays for in vivo electrophysiological interfacing. *Adv. Mater.* **29**, 1702800 (2017).
81. Huang, S., Liu, Y., Zhao, Y., Ren, Z. & Guo, C. F. Flexible electronics: stretchable electrodes and their future. *Adv. Funct. Mater.* **29**, 1805924 (2019).
82. Ling, Y. et al. Disruptive, soft, wearable sensors. *Adv. Mater.* **32**, 1904664 (2020).
83. Yokus, M. A., Songkakul, T., Pozdin, V. A., Bozkurt, A. & Daniele, M. A. Wearable multiplexed biosensor system toward continuous monitoring of metabolites. *Biosensors Bioelectron.* **153**, 112038 (2020).
84. Li, Q., Ran, Z., Ding, X. & Wang, X. Fabric circuit board connecting to flexible sensors or rigid components for wearable applications. *Sensors* **19**, 3745 (2019).
85. Chen, X., Rogers, J. A., Lacour, S. P., Hu, W. & Kim, D.-H. Materials chemistry in flexible electronics. *Chem. Soc. Rev.* **48**, 1431–1433 (2019).
86. Gao, W., Ota, H., Kiriya, D., Takei, K. & Javey, A. Flexible electronics toward wearable sensing. *Acc. Chem. Res.* **52**, 523–533 (2019).
87. Luebberding, S., Krueger, N. & Kerscher, M. Mechanical properties of human skin in vivo: a comparative evaluation in 300 men and women. *Skin Res. Technol.* **20**, 127–135 (2013).
88. Halligan, M. S. *Maximum crosstalk estimation and modeling of electromagnetic radiation from PCB/high-density connector interfaces* (Missouri University of Science and Technology, 2014).
89. Lu, N., Wang, X., Suo, Z. & Vlassak, J. Metal films on polymer substrates stretched beyond 50%. *Appl. Phys. Lett.* **91**, 221909 (2007).
90. Xiang, Y., Li, T., Suo, Z. & Vlassak, J. J. High ductility of a metal film adherent on a polymer substrate. *Appl. Phys. Lett.* **87**, 161910 (2005).
91. Fernandes, D. F., Majidi, C. & Tavakoli, M. Digitally printed stretchable electronics: a review. *J. Mater. Chem. C* **7**, 14035–14068 (2019).
92. Hsu, Y.-Y., Gonzalez, M., Bossuyt, F. & Vanfleteren, J. & De Wolf, I. Polyimide-enhanced stretchable interconnects: design, fabrication, and characterization. *IEEE Trans. Electron Devices* **58**, 2680–2688 (2011).
93. Linder, V., Gates, B. D., Ryan, D., Parviz, B. A. & Whitesides, G. M. Water-soluble sacrificial layers for surface micromachining. *Small* **1**, 730–736 (2005).
94. Topsoe, H. Geometric factors in four point resistivity measurement. *Bulletin* **472**, 63 (1968).
95. Smits, F. Measurement of sheet resistivities with the four-point probe. *Bell Syst. Tech. J.* **37**, 711–718 (1958).

ACKNOWLEDGEMENTS

This work was sponsored by a Center-to-Centre grant from the National Science Foundation (EEC1160483) through the NSF Nanosystems Engineering Research Center (NERC) for Advanced Self-Powered Systems of Integrated Sensors and Technologies (ASSIST). This work was performed in part at the Chapel Hill Analytical and Nanofabrication Laboratory (CHANL) and the Analytical Instrumentation Facility (AIF) at North Carolina State University, which are members of the North Carolina Research Triangle Nanotechnology Network (RTNN) which is supported by the National Science Foundation (ECCS2025064) as part of the National Nanotechnology Coordinated Infrastructure (NNCI). The authors also wish to acknowledge the Molecular Education, Technology, and Research Innovation Center (METRIC) and the Khan Group at North Carolina State University.

AUTHOR CONTRIBUTIONS

M.D., S.M., and B.T. conceived the presented concept and designed experiments. B.T. performed all experiments. J.T. and M.W. acquired and processed electrical characterization data. S.R. and B.T. acquired tensile and thermal degradation data. K.K., E.D, and O.N. assisted with data acquisition. J.T. designed the op-amp circuit, provided expertise on electrical measurements, and advised on soldering methodology. B.T., S.M. and M.D. wrote the paper manuscript with input from all authors.

COMPETING INTERESTS

The authors declare no competing interests.

ADDITIONAL INFORMATION

Supplementary information The online version contains supplementary material available at https://doi.org/10.1038/s41528-023-00258-z.

Correspondence and requests for materials should be addressed to Stefano Menegatti or Michael A. Daniele.